JACS
JOURNAL OF THE AMERICAN CHEMICAL SOCIETY
pubs.acs.org/JACS
Article

Nanobubble Nucleation and Dissolution Near the Anatase (101)−Water Interface

Pengchao Zhang, Yawen Gao, Changsheng Chen, Xiangdang Guo, Chao Sun,* and Xuefei Xu*

Cite This: J. Am. Chem. Soc. 2026, 148, 18507−18517
Read Online
ACCESS | Metrics & More | Article Recommendations | Supporting Information

ABSTRACT: In gas-involving (photo)electrochemical systems, nanoscale bubbles generate and enrich near the electrode−liquid interface, influencing interfacial transport and reactivity. However, it remains unclear how the solid−liquid interfacial microenvironment governs nanobubble evolution at the microscopic level. In this work, we perform deep potential molecular dynamics simulations with enhanced-sampling to investigate nucleation, dissolution, and detachment of nitrogen nanobubbles near the anatase (101)−water interface under neutral, acidic, and alkaline conditions. Our results show that the undercoordinated titanium and oxygen sites on the anatase (101) surface promote water dissociation, changing local ionic microenvironments. The resulting free hydroxide ions accumulate near the nanobubble surface, yielding a system-dependent negative zeta potential. The zeta potential of the nanobubble in the anatase−saline system is less negative than in other systems, due to the screening of locally paired sodium and chloride ions near the nanobubble surface. The dissolution barrier of nanobubbles shows a good linear positive correlation with the magnitude of zeta potential. This finding is further supported by the modeling with the Epstein−Plesset equation and the simulated bubble surface charge, as well as the experimental observations from nanoparticle tracking analysis and dynamic light scattering. The nucleation barriers are increased in systems with the anatase (101) surface compared to the anatase-free systems but are less sensitive to the acid−base strength. A significantly lower nucleation barrier in the anatase-saline system is attributed to the salting-out effect. The present study provides insights into nanobubble evolution near solid−liquid interfaces, with implications for bubble management in energy conversion systems.

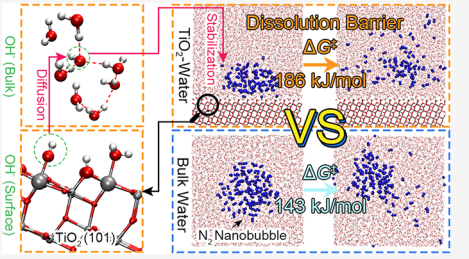

INTRODUCTION

Bubble management has recently received special attention as an important approach of improving energy and chemical conversion systems.[1,2] In both gas-evolving and gas-consuming (photo)electrochemical systems, bubbles that populate near the micro(nano)structured electrode surface may modify mass-transfer pathways, alter catalytic surface area, and reshape local ionic strength and pH, thereby altering efficiency and selectivity of (photo)electrochemical processes.[1,2] Understanding bubble nucleation,[3−5] growth,[6] coalescence,[7,8] detachment,[9] and dissolution[10−14] at the solid−liquid interfaces is therefore crucial for improving system performance.

Titanium dioxide (TiO_2), a prototypical oxide semiconductor, is one of the most widely used electrode materials in (photo)electrochemical systems, for example, the (photo)-electrochemical nitrogen reduction reaction (NRR) to produce ammonia[15,16] or water (photo)electrolysis to produce hydrogen.[17,18] In practical TiO_2-based NRR systems, a continuous stream of N_2 is often bubbled near the electrode, inevitably forming solid−liquid−gas three-phase contact regions populated by micro- and nanoscale bubbles.[19] In water electrolysis, gas bubbles are generated in situ at TiO_2-containing electrode surfaces. The adhesion of gas bubbles to the electrode surface reduces the electrochemically active area and hinders ion transport, leading to increased overpotentials and lower efficiency.[1] These observations underscore the broader importance of understanding and controlling gas bubble dynamics at TiO_2 electrode−electrolyte interfaces. Therefore, in this work, we focus on the evolution dynamics of N_2 gas nanobubbles near the TiO_2−water interface.

The basic properties of gas bubbles, in particular the stability of nanobubbles, remain the subject of active discussion. Classical theory suggests short-lived nanobubbles. According to the Epstein−Plesset description, the nanobubbles dissolve on millisecond time scales due to rapid diffusive outflux driven by Laplace pressure.[20] However, in apparent contradiction to this expectation, both surface nanobubbles and bulk nanobubbles have been observed to persist for hours or longer under ambient conditions.[3,21−28] For the stability of surface nanobubbles, experiments and theory have largely converged on a pinning−supersaturation mechanism, that is, the bubble is stabilized by the contact-line pinning in the condition of gas

Received: March 15, 2026
Revised: April 2, 2026
Accepted: April 15, 2026
Published: April 24, 2026

supersaturation.[29−32] Relatively, bulk nanobubbles are less well understood, and their observed longevity is often associated with interfacial charging.[25−27,33] A recurring observation is that nanobubble suspensions exhibit a negative zeta potential over a broad pH range from 4 to 12,[25,27,34−36] and that the zeta potential becomes more negative with increasing pH.[37,38] In addition, the stability of bulk nanobubbles is also sensitive to the electrolyte composition.[11] This sensitivity mainly originates from the dual role of electrolytes: electrolytes not only shift gas solubility in the bulk water but also regulate interfacial charge and mass transport at gas−water interfaces. From a thermodynamic perspective, electrolytes often reduce gas solubility via the salting-out effect,[39,40] which can increase the degree of supersaturation at a fixed dissolved-gas content and thereby favor bubble nucleation. In addition, recent studies on bulk nanobubbles suggested that nanobubble surface charges arising from ion adsorption can slow gas diffusion across the bubble surface,[27,33,41] thereby enhancing nanobubble stability.

It is well recognized that the TiO_2−water interface is not electrostatically inert. A body of evidence has shown that the TiO_2 surface carries a pH-dependent surface charge through amphoteric hydroxylation reactions.[42−46] Molecular simulations at atomic levels[42−44] and surface-specific experiments[45,46] further revealed that TiO_2 surfaces in contact with water typically exhibit mixed adsorption of water molecules and ions.

Thus, it is natural to ask how nanobubbles nucleate, evolve, detach, and ultimately dissolve in the vicinity of a charged TiO_2−water interface. In particular, it remains unclear how local ionic environments shaped by the TiO_2−water interface chemistry feed back on the nucleation barrier and the dissolution kinetics of nanobubbles.

Addressing this question requires a framework that can treat gas−liquid interfacial physics and solid−liquid interfacial chemistry on the same footing. Although experiments can reveal variations of bubble populations with electrolyte composition and pH, they do not readily provide molecular-level insights into the complex mechanisms that control nanobubble evolution.[26−28,47] In this regard, complementary molecular simulations are essential for identifying microscopic evolution pathways and for quantifying the underlying thermodynamic driving forces.

Molecular dynamics (MD) simulations with classical force fields, including coarse-grained models, have been widely used to study the nanobubble behavior.[3,7,8,10−14,28,48] However, empirical force fields are not designed to reliably describe bond-breaking and bond-forming processes that are central to oxide−water interface reactions, such as interfacial water dissociation and proton transfer via the Grotthuss mechanism.[49−51] Recently, machine learning interatomic potentials have provided a promising solution. In particular, the deep potential (DP) molecular dynamics (DPMD) approach[52,53] offers a near-*ab initio* accuracy at a computational cost closer to the classical MD, allowing chemically faithful simulations of aqueous oxide surfaces. Nevertheless, generally, direct DPMD trajectory simulations are hardly able to capture events like nanobubble nucleation, dissolution, and detachment, because these processes are activated events that occur too rarely on the time scales accessible to be observed by unbiased simulations. Enhanced sampling techniques[54−57] are therefore required to simulate these processes and to reconstruct the corresponding free energy landscape.

In this work, we investigate the evolution of N_2 nanobubble near the anatase TiO_2 (101)−water interface (hereafter referred to as the TiO_2−water interface) primarily through enhanced-sampling DPMD simulations, combined with experimental validation. Based on this combined investigation, we quantify the thermodynamic and kinetic information associated with nanobubble nucleation, dissolution, and detachment near the TiO_2 surface in various environments, including pure water and acidic, basic, and salt solutions. The present study links the interfacial ionic microenvironment to dynamically controlled nanobubble evolution and provides a guideline for regulating gas accumulation and release near TiO_2−water interfaces in gas-involving electrochemical environments.

■ METHODS

Deep Potential Model Training

Considering that the energy component of the deep potential model depends on local atomic environments, it is crucial to construct representative subsystems (Table S1 in the Supporting Information) that capture the relevant structural diversity. Part of the configurations used in this study were adapted from previously developed data sets, including N_2 molecules in bulk water containing self-ions[33,51] and configurations representing the TiO_2−water interface.[44] To accurately describe the dynamic evolution of N_2 nanobubbles near the TiO_2−water interface, additional configurations were generated. These new data incorporate the local atomic environments of N_2 molecules in neutral, acidic, and basic aqueous solutions adjacent to the TiO_2 surface.

The final DP model was trained using the DeePMD-kit package[53,58] based on a data set containing 144,215 configurations (Figure S1a) and validated against an independent test set. All reference energies and forces were obtained from SCAN[59] functional-based DFT calculations performed in VASP.[60,61] To enable efficient large-scale molecular dynamics simulations, the trained DP model was further compressed.[62] Root-mean-square errors (RMSEs) of the compressed[62] DP model are 1.21 meV/atom for energies and 43 meV/Å for forces relative to the SCAN results (Figure S1b,c), which confirm its accuracy.

Enhanced Sampling

The collective variable (CV) based umbrella sampling (US)[63] or on-the-fly probability enhanced sampling (OPES)[64−66] method was used in DPMD simulations with the PLUMED package[67] to investigate the dynamics of nanobubble, including the formation, growth, and detachment from the TiO_2 surface. We designed two CVs to capture the slow collective motions governing the N_2 nanobubble evolution. Specifically, we used CV Δz to describe the vertical distance between the nanobubble centroid and the TiO_2 surface in US simulations and CV **s** to characterize the formation and growth of N_2 molecular cluster in OPES simulations.[68]

This CV **s** is formulated based on an adjacency matrix **M**, in which each matrix element M_{ij} quantifies the degree of connection between particles. Here, each particle corresponds to the centroid of a N_2 molecule, which is defined as the midpoint between its two nitrogen atoms. The CV **s** is then expressed as the total coordination number of all centroids that belong to the largest connected molecular cluster:

$$\mathbf{s} = \sum_{i=1}^{N_1} \sum_{j=1}^{N} M_{ij} \tag{1}$$

where the first summation runs over the N_1 centroids that form the largest cluster, and the second summation extends over all N centroids present in the system.

DPMD Simulation

Deep potential molecular dynamics simulations with the US or OPES method were performed using the LAMMPS package[69] to investigate

https://doi.org/10.1021/jacs.6c05480
J. Am. Chem. Soc. 2026, 148, 18507−18517

the dynamic behavior of N_2 nanobubbles near the anatase (101)−water interface in neutral, acidic, and alkaline aqueous environments. For simulations of the TiO_2−pure water system, an initial nanobubble containing 102 N_2 molecules was embedded in a periodic simulation box containing 7,401(16,144) H_2O molecules and an anatase $Ti_{1920}O_{3840}$ slab. The systems TiO_2−NaOH, TiO_2−HCl, and TiO_2−NaCl were constructed by introducing 0.24 M solutes into the aqueous phase of the TiO_2−(pure) water system. For comparison and validation, DPMD simulations were also conducted in bulk Water and NaOH solution systems without the TiO_2 slab. The initial atomic arrangements were generated using PACKMOL,[70] and a summary of all simulation systems is provided in Table S2.

All simulations were carried out in the isothermal−isobaric (*NPT*) ensemble at a temperature of 330 K and a pressure of 1 atm. The simulation temperature was set 30 K above ambient, because prior studies showed this slight temperature rise in SCAN-based molecular simulations helped to approach the liquid water properties at 300 K.[71] Temperature and pressure were controlled using the Nosé−Hoover thermostat and barostat,[72,73] with damping constants of 0.1 and 1 ps, respectively. Independent trajectories were generated for each system, and each trajectory was run over at least 10 ns with a time step of 1 fs.

Further details of the simulations can be found in the Supporting Information (SI).

Experimental Details

Three types of aqueous samples were prepared in this study: (i) bulk nanobubble suspensions, (ii) TiO_2 nanoparticle suspensions, and (iii) bulk nanobubble suspensions first prepared and then mixed with TiO_2 nanoparticles. Bulk nanobubbles were generated using an ultrasonic cavitation system (VCX 750 W, Sonics & Materials, USA), with each batch prepared at a volume of 80 mL. The ultrasonication duration and total energy input were maintained at 20 min and 18.5 kJ, respectively. Anatase-phase TiO_2 nanoparticles (purity ≥ 99.99% metals basis, nominal size ≤ 50 nm) were purchased from Shanghai Aladdin Biochemical Technology Co., Ltd. The TiO_2 concentration was fixed at 5 μg/mL for suspensions prepared in both ultrapure water and nanobubble water. After generating the nanobubble suspension, the nanoparticle dispersion was added and mixed to obtain the final nanobubble−nanoparticle mixture for subsequent characterization.

Nanobubble size distributions were determined using nanoparticle tracking analysis, implemented via a custom dark-field imaging system built around an Olympus IX73 inverted microscope.[74] A 20× objective lens (depth of field: 6.526 μm) and a CMOS camera (Basler acA2440-35uc, 2448 × 2048 pixels; spatial resolution: 172.5 nm/pixel; 30 frames per second) were used for image and video acquisition. A 532 nm continuous-wave laser (SUM-EMERP-3, China) was coupled through a prism-edged optical flat to illuminate nanosubstances within a quartz visualized chamber. For each sample, at least three video sequences (≥45 s each) were recorded. Number concentrations of nanobubbles were estimated by counting scattering features in the recorded frames, and particle trajectories were analyzed using the NanoTrackJ plugin in ImageJ/Fiji to calculate size distribution from diffusion-based tracking.[28,75] In the mixed nanobubble and TiO_2 system, nanoparticle tracking analysis shows number concentration and size distribution of dispersed objects. Since NTA cannot distinguish nanobubbles from solid particles, these results should be interpreted as indicating an overall characterization of the dispersed population.

The pH values of samples were measured using a multiparameter system (S975-uMix, Mettler Toledo, Switzerland). Zeta potential of aqueous samples was measured based on the electrophoretic mobility with a ZEN3700 Zetasizer Nano ZSE instrument (Malvern Instruments, UK). Before each measurement, the suspension was injected into a clean U-shaped capillary cell and equilibrated at room temperature.[76] For each sample, six replicate measurements were performed, and the standard deviation was calculated from the resulting data.

RESULTS AND DISCUSSION

Propensity of Nanobubble toward the Anatase (101)−Water Interface

Since the present study focuses on the dynamic behavior of a single N_2 nanobubble near the anatase (101)−water interface, we first investigate the preference of the nanobubble toward the interface. Figure 1 presents the free energy surface (FES)

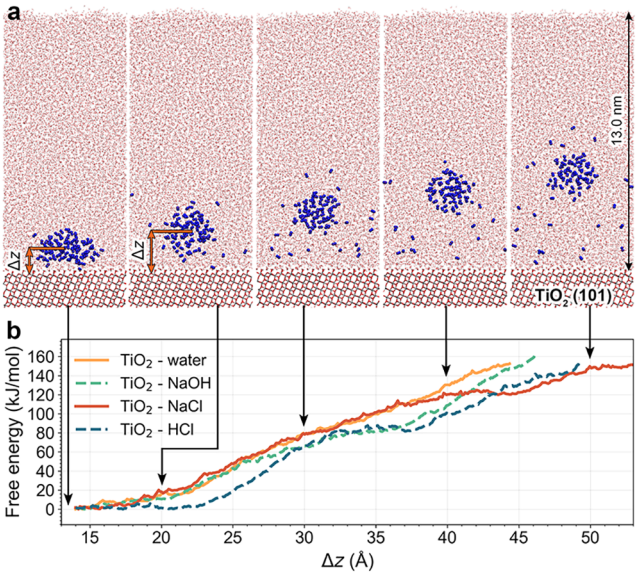

Figure 1. Nanobubble detachment dynamics and free energy surfaces. (a) Representative snapshots showing the detachment of an N_2 nanobubble from the TiO_2 surface into the solution. (b) One-dimensional free energy profiles of nanobubble detachment under different solution conditions, projected onto the CV Δz, which represents the vertical distance between the nanobubble centroid and the TiO_2 surface.

of a N_2 nanobubble (about 3 nm in diameter) departure from the TiO_2 surface toward the aqueous phase as a function of the normal distance to the surface (z), as well as representative snapshots of the dynamic process, which show that the nanobubble remains compact when its center of mass is pulled upward (Figure 1a). The free energies of the systems increase nearly monotonically from $z \approx 14$ Å (the approximate position of the TiO_2−water interface) to $z \approx 45$−50 Å, and the increases of the free energies are about 150 kJ/mol (Figure 1b). This monotonic rise indicates that for the nanobubble, the interfacial adsorption state is thermodynamically preferred, and the detachment into the bulk is strongly disfavored. Notably, the profiles show weak sensitivity to the solution. The four investigated systems (TiO_2−water, TiO_2−NaOH, TiO_2−HCl, and TiO_2−NaCl as listed in Table S2), display similar FESs (including both trend and magnitude) along z. Because these distinct solution environments can affect the interfacial charge and water structure differently, the observed similarity of energy profiles suggests that the detachment thermodynamics is mainly dominated by generic interfacial stabilization; that is, the free energy gain is obtained through the interaction of the nanobubble with the interface and is less affected by specific ionic conditions.

In addition, we observe an interfacial water film with a thickness of only a few angstroms that separates the nanobubble from the TiO_2 surface at the minimum of free

https://doi.org/10.1021/jacs.6c05480
J. Am. Chem. Soc. 2026, 148, 18507−18517

energy (zero point of free energy) in Figure 1. This is due to the hydrophilic nature of the anatase (101) surface, and with the approaching of nanobubble toward the surface, the gradually formed ultrathin water film between the bubble and the surface can be sustained by a disjoining pressure arising from van der Waals interactions across the film.[77] The water film prevents the nanobubble from direct contact with the TiO_2 surface, that is, avoids the formation of surface nanobubble.

Note that although we observed a strong preference of the nanobubble staying near the interface, this does not mean that bubble detachment cannot occur. The nanobubble addressed here may be too small for buoyancy to provide a substantial driving force, and so the departure is not expected to follow the same pathways as larger bubbles. In practical (photo)-electrochemical systems, bubble detachment from the electrode surface is commonly observed only after bubbles have grown or coalesced to larger sizes (micrometer scale), and the detachment of micrometer-size bubbles is promoted by macroscopic driving forces, including buoyancy, shear, and Marangoni stresses,[1,9] which largely determine the diameters of the detached bubbles and release frequencies.[1]

Evolution of the N_2 Nanobubble near the Anatase (101)–Water Interface

We now examine the nucleation and dissolution dynamics of N_2 nanobubble near the TiO_2–water/electrolyte interface. Figure 2 shows one-dimensional FES profiles of nanobubbles in various environments projected along the CV **s**. For aqueous systems without the TiO_2 surface (Figure 2a), the profiles clearly resolve three characteristic states of nanobubble along **s**: A fully dissolved state (labeled as DS) at $\mathbf{s} \approx 0$, a critical nucleus (labeled as CN) at $120 < \mathbf{s} < 220$, in which a small nanobubble coexists with dissolved gas, and an intact nanobubble state (labeled as IS) at $\mathbf{s} > 400$. The representative snapshots of the three states are also provided in Figure 2a. The pure water system yields a nucleation barrier of 141 kJ/mol and a dissolution barrier of 144 kJ/mol. The NaOH solution system shows a lower nucleation barrier of 108 kJ/mol and a higher dissolution barrier of 191 kJ/mol. Furthermore, the nucleation free energy (ΔF_{IS-DS}), defined as the free energy difference between the fully dissolved and intact bubble states, changes significantly from about −3 kJ/mol in Water to about −83 kJ/mol in NaOH (Figure 2a and Table 1). These results indicate that not only do alkaline conditions dynamically promote the formation of nanobubble by reducing the activation free energy barrier, but they also stabilize the nanobubble better from a thermodynamic perspective. This agrees with the experimental observation of faster nucleation and greater persistence of nanobubbles under basic conditions.[78] The present bulk water results are also consistent with our previous unbiased DPMD simulations.[33] Specifically, the unbiased trajectories reproduced the qualitative pH-dependent evolution trend, in which nanobubbles show limited dissolution and enhanced persistence under alkaline conditions, whereas acidic conditions promote dissolution. The present enhanced-sampling simulations further provide a quantitative characterization in free energy along the whole evolution process that is not accessible from unbiased runs, by resolving the critical nucleus state and quantitatively determining both the nucleation and dissolution barriers.

Figure 2b presents the FES plots of nanobubbles near the TiO_2–water/electrolyte interfaces and the associated snapshots. Near the TiO_2–water interface, the fully dissolved state of nanobubble is also less stable than the intact bubble state with a free energy difference of 8 kJ/mol, and the barriers are 178 kJ/mol for nucleation and 186 kJ/mol for dissolution, both larger than those in bulk Water. Near the TiO_2–NaOH interface, the same relative stability is observed, with a nucleation free energy of −25 kJ/mol, a nucleation barrier of

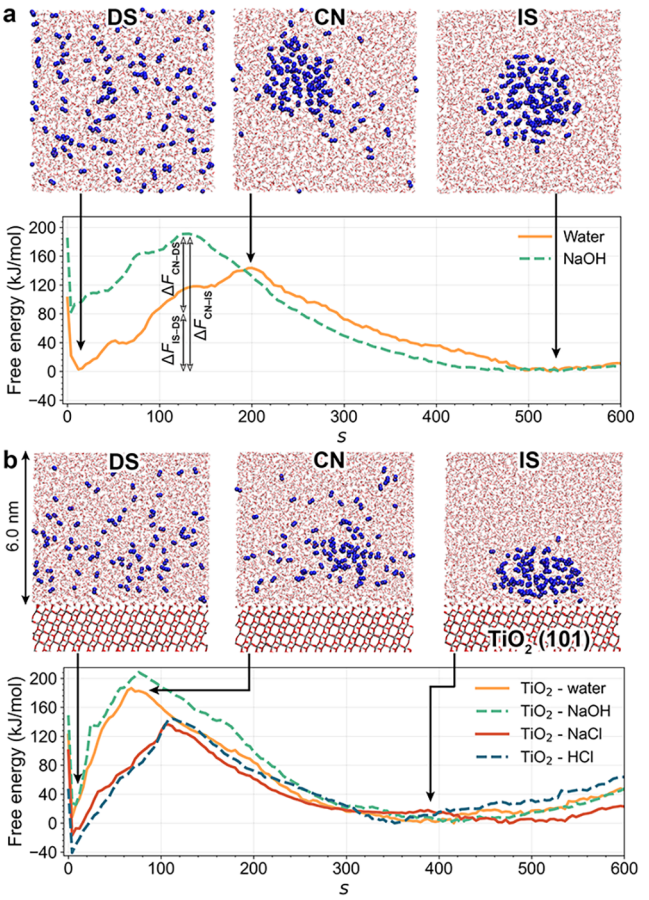

Figure 2. Dynamic snapshots and free energy surfaces of the N_2 nanobubble nucleation and dissolution. Representative snapshots and corresponding one-dimensional free energy profiles of the N_2 nanobubble along the CV **s** are presented for two systems: (a) aqueous systems without TiO_2, and (b) the TiO_2-containing systems. The snapshots illustrate three characteristic stages of nanobubble evolution: the fully dissolved state (DS), the critical nucleus (CN), and the intact state (IS). The nucleation free energy (ΔF_{IS-DS}), nucleation barrier (ΔF_{CN-DS}), and dissolution barrier (ΔF_{CN-IS}) are illustrated with the NaOH aqueous system as a representative example for clarity. Specific values are given in Table 1.

Table 1. Nucleation Free Energy (ΔF_{IS-DS}), Nucleation Barrier (ΔF_{CN-DS}), and Dissolution Barrier (ΔF_{CN-IS}) of Nanobubble Evolution

	free energy (kJ/mol)		
system	nucleation free energy	nucleation barrier	dissolution barrier
TiO_2–water	−8	178	186
TiO_2–NaOH	−25	183	208
TiO_2–HCl	40	185	145
TiO_2–NaCl	17	153	136
water	−3	141	144
NaOH	−83	108	191

https://doi.org/10.1021/jacs.6c05480
J. Am. Chem. Soc. 2026, 148, 18507−18517

183 kJ/mol, and a dissolution barrier of 208 kJ/mol. These results indicate that in both systems, the interaction of nanobubble with the interface reduces the thermodynamic stability of nanobubble and slows the dynamic interconversion between the dissolved state and intact nanobubble state. Unlike the four systems mentioned above, the TiO_2−HCl and TiO_2−NaCl interface systems favor the dissolved state both thermodynamically and dynamically. The nucleation free energies are 40 and 17 kJ/mol, respectively; the dissolution barriers are 145 and 136 kJ/mol, respectively.

For convenience of comparison, Table 1 further tabulates the nucleation free energies, the nucleation free energy barriers, and the dissolution free energy barriers of all these investigated systems. We notice that the nucleation barriers are larger in all systems containing TiO_2 than in the TiO_2-free systems, which is consistent with the point of view that hydrophilic surfaces suppress heterogeneous bubble nucleation.[79] Across the TiO_2−containing systems, the nucleation barriers follow the order of TiO_2−HCl ≳ TiO_2−NaOH ≳ TiO_2−water > TiO_2−NaCl, whereas the dissolution barriers follow TiO_2−NaOH > TiO_2−water > TiO_2−HCl ≳ TiO_2−NaCl. Thus, relatively, TiO_2−NaOH interface stabilizes the nanobubbles both kinetically and thermodynamically, as evidenced by a higher dissolution free energy barrier and a more negative nucleation free energy. In contrast, chloride-containing interface environments thermodynamically favor the dissolved state and lower the free energy barrier for nanobubble dissolution.

TiO_2 Surface-Modulated Microenvironments

To understand the different thermodynamics and dynamics of nanobubble nucleation and dissolution observed in the investigated systems, we investigated the microscopic structures near the anatase (101) surface in various solutions, in particular focusing on the formation and distribution of ions at the anatase (101)−water/electrolyte interface.

As illustrated in Figure 3a, undercoordinated atoms on the anatase (101) surface, specifically 5-fold coordinated titanium (Ti_{5c}) and 2-fold coordinated oxygen (O_{2c}), can adsorb water molecules and facilitate their dissociation, leading to the coadsorption of OH^- and H^+ on the surface. Figure 3a(I) shows that the yielded OH^- and H^+ ions are bound to Ti_{5c} and O_{2c} sites, respectively. Previous studies[42−44] have described this process as a concerted, hydrogen-bond−mediated proton-transfer pathway that proceeds via a Grotthuss mechanism.[49,50]

Although water dissociation on the anatase (101) surface is well established, our simulations observed the presence of OH^- ions in the bulk water of the nominally TiO_2−pure water system. This observation motivates a mechanistic analysis of how bulk OH^- is generated from interfacial reactions.

Figure 3b summarizes the species transition matrix in the TiO_2−water system among adsorbed water molecules (H_2O (surf)) and adsorbed OH^- ions (OH^- (surf)) on the TiO_2 surface and free OH^- ions in bulk water (OH^- (bulk)), where the species identity is tracked by the oxygen index (see more details about the transition matrix in the SI). The matrix shows that all three species largely preserve their identities with probabilities exceeding 0.97, indicating that the interfacial speciation is stable. A small but non-negligible fraction (0.028) of surface hydroxide oxygens are protonated and reassigned from OH^- (surf) to H_2O (surf), which signals proton transfer at the interface (Figure 3c). Decomposing this 0.028 probability reveals two distinct PT pathways. In the first pathway, denoted PT (surf), a neighboring H_2O (surf) donates a proton to the OH^- (surf), exchanging the adsorption sites of OH^- (surf) and H_2O (surf). In the second pathway, denoted PT (bulk), the OH^- (surf) abstracts the proton of a nearby free water molecule that is unbound to the TiO_2 surface. This step neutralizes the surface OH^- (surf) to form a H_2O (surf) and generates a free OH^- (Figure 3a(II)). Once generated, the free OH^- can migrate away from the surface region toward the bulk water along hydrogen-bonded water networks through a Grotthuss-like mechanism, as illustrated in Figure 3a(III). This PT (bulk) channel therefore provides a direct route for producing bulk OH^-. H_3O^+ ions are also occasionally detected in the bulk (Figure 3a(IV)) of the pure water system, which are mainly from the self-ionization reaction of bulk water.

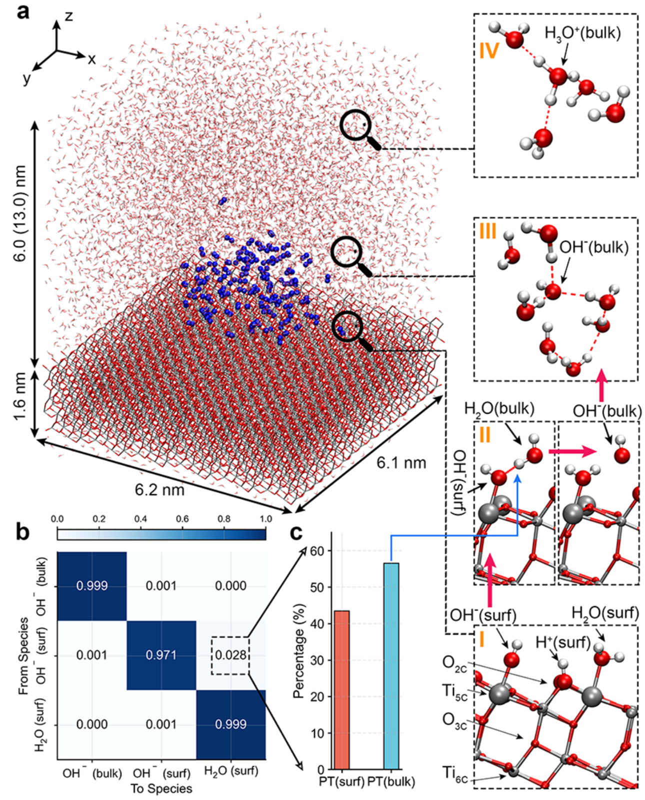

Figure 3. Schematic structure of the TiO_2 system and ion transition mechanism. (a) Three-dimensional schematic of an N_2 nanobubble located near the anatase (101)−water interface. The magnified subfigures from bottom to top illustrate: (I) the interfacial region contains undercoordinated surface Ti_{5c} and O_{2c} atoms that adsorb OH^-, H^+, and H_2O species, whereas Ti_{6c} and O_{3c} atoms are the fully coordinated atoms in the inner layer of TiO_2. (II) the proton-transfer process from H_2O (bulk) to OH^- (surf), resulting in the exchange of their identities to OH^- (bulk) and H_2O (surf); (III) OH^- and (IV) H_3O^+ ions in the bulk region and their surrounding water molecules. (b) Visualization of the transition matrix describing the conversion probabilities among H_2O (surf), OH^- (surf), and OH^- (bulk) species in the TiO_2−water system. The color bar indicates the normalized transition probabilities, where each row is normalized independently. (c) Schematic illustration of the proton-transfer (PT) pathways from OH^- (surf) to H_2O (surf). PT (surf) and PT (bulk) represent proton transfers involving H_2O molecules located at the surface and in the bulk region, respectively.

When the production and interconversion of ions in the interface reach a dynamic steady state, the overall ionic composition becomes stable. Figure 4a shows the equilibrium ionic concentrations of the investigated systems, as well as

https://doi.org/10.1021/jacs.6c05480
J. Am. Chem. Soc. 2026, 148, 18507−18517

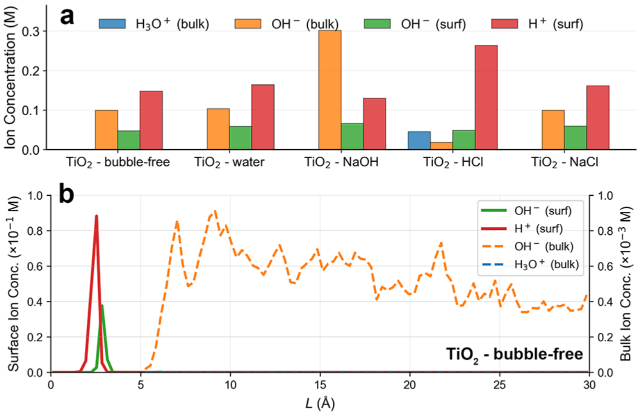

Figure 4. Concentration distribution of ions. (a) Concentration profiles of H^+, H_3O^+ and OH^- ions in the five TiO_2-containing systems. (b) Concentration profiles of H^+, H_3O^+, and OH^- ions as a function of the vertical distance $L = z_{ion} - z_{surface}$ from the TiO_2 surface of the TiO_2−bubble-free system, where $z_{surface}$ represents the mean position of the surface O_{2c} sites.

those of a bubble-free TiO_2−water system (which removes the nanobubble from the TiO_2−water system and will be called TiO_2−bubble-free) for comparison. The TiO_2−bubble-free, TiO_2−water and TiO_2−NaCl systems exhibit nearly identical ionic concentrations, each containing approximately 0.15−0.16 M of surface H^+, 0.05−0.06 M of surface OH^-, and 0.10 M of bulk OH^-, while bulk H_3O^+ remains negligible. It indicates that the presence of nanobubble has negligible influence on the water dissociation reactions on the anatase (101) surface, and the Na^+ and Cl^- ions have no influence either. For the electrolyte-containing TiO_2 systems, the initial solute concentration is 0.24 M. The anatase (101) surface changes the acid−base property of solutions, making the neutral aqueous solution become alkaline. In the TiO_2−NaOH system, the alkaline environment markedly enhances the OH^- concentration to about 0.30 M in the bulk and 0.07 M on the TiO_2 surface, accompanied by a slight reduction of surface H^+ to 0.13 M. In the acidic TiO_2−HCl system, the surface H^+ concentration increases substantially to 0.26 M, along with a low bulk H_3O^+ concentration of 0.05 M and a low surface OH^- concentration of 0.05 M. Interestingly, a very low concentration of bulk OH^- (0.02 M) is observed in the acidic system, and these bulk OH^- ions are generated by the PT (bulk) reaction mentioned earlier.

We also calculated the depth-resolved concentration profiles to further characterize the spatial distribution of ions, along the normal distance (L) from the TiO_2 surface for the bubble-free system (Figure 4b). The H^+ (surf) concentration reaches a maximum at $L \approx 2.5$ Å, while the OH^- (surf) concentration exhibits a prominent peak around 2.9 Å. OH^- (bulk) ions are predominantly distributed at $L > 5$ Å, whereas bulk H_3O^+ remains nearly absent.

Taken together, these findings indicate that the presence of anatase (101) surface changes ionic microenvironments, making the TiO_2−water and TiO_2−NaCl systems alkaline, the TiO_2−NaOH system more alkaline, and the TiO_2−HCl system close to neutral. The experimental pH results qualitatively support this conclusion. Pure water and water with bulk nanobubbles have nearly identical pH values of 5.960 and 5.958. After adding TiO_2 nanoparticles, the pH increases to 7.097 for TiO_2 suspensions and to 6.687 for TiO_2 and nanobubble suspensions. This restructuring of ionic microenvironments and change of the acid−base equilibrium might influence nanobubble nucleation and dissolution processes.

Ion-Modulated Nanobubble Evolution

The TiO_2 surface-reconstructed ionic microenvironments have a direct influence on the ionic distribution near the nanobubble surface and consequently affect the stability and evolution of nanobubble.

Figure 5 reports volume-normalized number-density profiles of bulk H_3O^+, OH^-, Na^+, and Cl^- as a function of the normal distance d from the N_2 nanobubble surface. Here, d is defined as the minimum distance between the ionic center of mass and the outermost nitrogen atoms of the largest N_2 cluster. The cluster is identified through a connectivity analysis.

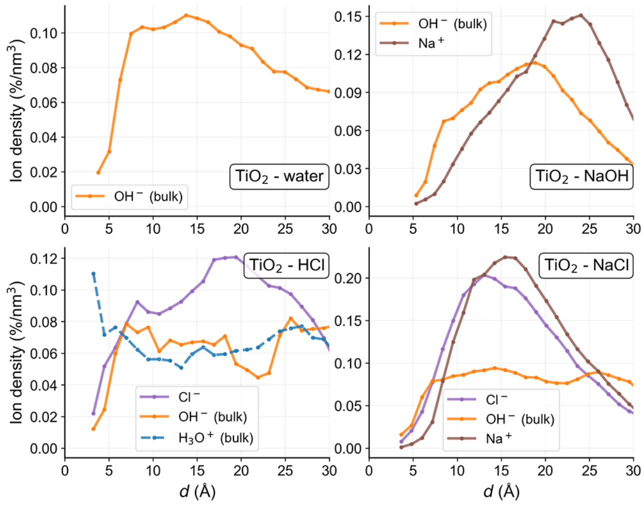

Figure 5. Spatial distribution of ions surrounding the nanobubble in the TiO_2-containing systems. Volume-normalized number density profiles of bulk H_3O^+, OH^-, Na^+, and Cl^- ions are shown as a function of the radial distance (d) from the N_2 nanobubble surface. Each profile is volume-normalized by averaging over concentric spherical shells of increasing mean radius from the nanobubble center.

Introducing TiO_2 into pure water creates an alkaline microenvironment for the nanobubble, so that in the TiO_2−water system, a negatively charged shell forms near the nanobubble surface with bulk OH^- as the dominant ions, peaking at $d \approx 9$−16 Å. Compared with TiO_2−water, the bulk OH^- distribution peak shifts to larger distances ($d \approx 19$ Å) in TiO_2−NaOH, which may arise from electrostatic attraction between OH^- and Na^+, given that Na^+ ions mainly enrich at $d \approx 24$ Å. In the region of $d \approx 5$−18 Å, the number density of OH^- remains higher than that of Na^+. This OH^--rich shell yields a negative interfacial potential and stabilizes the local hydrogen-bond network,[33] suppressing molecular exchange across the boundary and slowing gas outflux. Based on the Debye−Hückel approximation,[51,80] the cumulative zeta potentials ζ at a distance of $d = 2$ nm from the N_2 nanobubble surface for the TiO_2−NaOH and TiO_2−water systems are −4.0 and −2.7 mV, respectively. It well explains the larger dissolution barrier of nanobubble in TiO_2−NaOH (Table 1) than in TiO_2−water, and these results are consistent with prior simulations[33] and experimental trends[25,27,41,81] that nanobubbles are more persistent under more alkaline conditions.

Similar to the TiO_2−water system, there are some bulk OH^- ions in TiO_2−NaCl systems produced by the surface reaction

https://doi.org/10.1021/jacs.6c05480
J. Am. Chem. Soc. 2026, 148, 18507−18517

of TiO_2 which also show a distribution peak at $d \approx 9-16$ Å (Figure 5). The key differences in nanobubble stability and evolution between these two neutral TiO_2 systems are therefore the presence of NaCl. Figure 5 shows that the Na^+ and Cl^- in TiO_2−NaCl system mainly populate near the nanobubble with distinct peaks at $d \approx 15$ Å for Na^+ and at $d \approx 13$ Å for Cl^-. This ionic layer of Na^+ and Cl^- spanning $d \approx 9-16$ Å screens the interfacial charges,[41,82] weakens the net interfacial potential with a zeta potential ζ (−0.6 mV) less negative than that in the TiO_2−water system, leading to a remarkably lower dissolution barrier (Table 1). In addition, the elevated local ionic strength induces salting-out and lowers gas solubility,[39,40] which favors nanobubble nucleation and explains the much lower nucleation barrier (approximately 30 kJ/mol lower) than those of the other TiO_2-containing systems.

In the TiO_2−HCl system, the maximum H_3O^+ number density appears at $d \approx 3-5$ Å (Figure 5), consistent with our previous observation.[33,51] This interfacial enrichment of H_3O^+ perturbs the local hydrogen-bond network and thereby promotes nanobubble dissolution.[33] For $d > 5$ Å, bulk H_3O^+ and OH^- are both less abundant and nearly compensate for each other. The Cl^- ions are also populated near the nanobubble surface with a relatively wide distribution at $d \approx 5-30$ Å (Figure 5), which neutralizes the weak positive charges of the interfacial accumulated H_3O^+, leading to a zeta potential ζ of −1.6 mV. Accordingly, as shown in the free-energy profile (Figure 2b), the dissolved state of nanobubble in the TiO_2−HCl system is remarkably preferred, as well as with a lower dissolution barrier.

Figure 6a clearly shows the linear correlation between the cumulative zeta potentials ζ and the dissolution barriers ΔF of nanobubbles in all the TiO_2−containing systems. In particular, a more negative zeta potential corresponds to a higher barrier

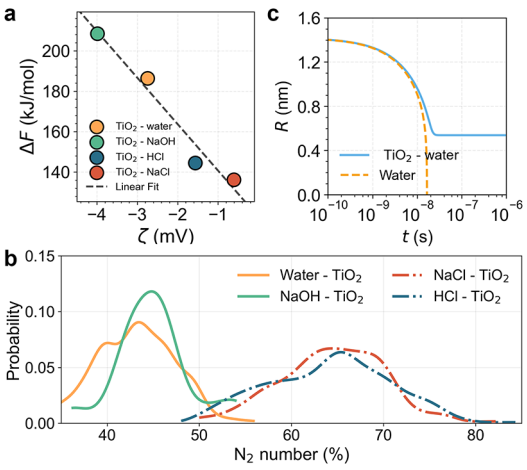

Figure 6. Zeta potential, critical nucleus ensemble, and time-evolution of the N_2 nanobubble in different systems. (a) Correlation between the Gibbs free energy barrier (ΔF) of dissolution and the cumulative zeta potential (ζ) evaluated at a distance of $d = 2$ nm from the N_2 nanobubble surface. The dashed line indicates the linear fit. (b) Probability distribution of the fraction of N_2 molecules within the critical nucleus ensemble of the nanobubble. Configurations included in this ensemble were identified based on the value of the CV **s** corresponding to the critical nucleus shown in Figure 2. (c) Theoretical dynamic evolution of N_2 nanobubble radius R with time in water with(out) TiO_2.

for nanobubble decay. These results support that bulk OH^- and H_3O^+ exert dominant yet opposite effects on nanobubble evolution: OH^- stabilizes the bubble, whereas H_3O^+ promotes dissolution.[33] By contrast, Na^+ and Cl^- can cooperatively influence the evolution dynamics by tuning the interfacial electrostatic environment and by the salting-out effect. Such cooperative behavior is not expected when only one of Na^+ or Cl^- is present, as in alkaline or acidic systems. In the TiO_2−NaCl system, the number-density profiles of Na^+ and Cl^- are similar, presenting local Na^+−Cl^- pairing around the nanobubble. The ion-pair separations (~2.8 to 4.5 Å) are energetically favorable,[83] which maintains spatial correlation between cations and anions near the interface and enhances charge screening. This behavior differs from TiO_2−NaOH, where Na^+ is mainly distributed at $d > 20$ Å, and from TiO_2−HCl, where Cl^- is more broadly distributed (Figure 5).

We further analyzed the structural characteristics of the critical nucleus (CN) state connecting the intact bubble and the dissolved state by quantifying the fraction of N_2 molecules in the CN ensemble for the TiO_2-containing systems, and the results are shown in Figure 6b. For TiO_2−water, the CN distribution peaks at ~43% of the total N_2 population with a probability of ~0.09. In TiO_2−NaOH, the peak shifts slightly to ~45%, and the probability increases to ~0.12. By contrast, the CN peaks in TiO_2−HCl and TiO_2−NaCl correspond to a larger cluster fraction (~65%), accompanied by lower probabilities (~0.06) and broader distributions (Figure 6b). These CN characteristics are consistent with the order of dissolution barriers. The smaller sizes of CN in TiO_2−water and TiO_2−NaOH correspond to a higher free-energy cost for barrier crossing.

Classical Kinetic Modeling

The enhanced-sampling DPMD simulations and the above analysis revealed that interfacial charges (zeta potential) still play a dominant role in the evolution of nanobubble near the TiO_2 surface, which are regulated by the TiO_2 surface reactions in various solutions and the ionic propensity toward the nanobubble surface. We therefore investigated the time evolution of nanobubble dissolution by a classical kinetic modeling using the Epstein−Plesset relation[20] and the interfacial charge (Q) of the bubble extracted from the DPMD trajectory simulations for bulk water and TiO_2−water systems. Here, the use of the Epstein−Plesset relation is justified by the fact that the hydrophilic TiO_2 surface is separated from the nanobubble by a thin interfacial water film, so that the bubble remains in a bulk-like liquid environment.

Following our earlier derivation,[33] the dissolution rate is estimated as

$$\frac{dR}{dt} = \frac{D}{\rho}(c_1 - Hp_2)\left(\frac{1}{R} + \frac{1}{\sqrt{\pi Dt}}\right) \quad (2)$$

where R is the nanobubble radius, t is time, D is the diffusivity of N_2 in water, ρ is the gas density inside the nanobubble, c_1 is the dissolved N_2 concentration in the liquid, H is the Henry coefficient, and p_2 is the gas pressure inside the bubble obtained from mechanical equilibrium:[80]

$$p_1 + \frac{2\gamma}{R} = p_2 + \frac{Q^2}{32\pi^2\epsilon R^4} \quad (3)$$

where p_1 is the liquid pressure, γ is the surface tension, ϵ is the permittivity of the medium, and Q, taken as a trajectory-

https://doi.org/10.1021/jacs.6c05480
J. Am. Chem. Soc. 2026, 148, 18507−18517

averaged value, is the net ionic charge within d = 2 nm of the nanobubble surface.

The predicted evolution results are shown in Figure 6c. In bulk Water, the radius of the nanobubble decreases monotonically with time and vanishes at ~16 ns. In TiO_2−water, the decay is slower and reaches an arrested state at ~32 ns, with a finite radius of ~0.54 nm (a six-N_2 cluster). This kinetic modeling result is qualitatively consistent with the enhanced-sampling DPMD simulations, in the sense that both approaches show nanobubble dissolution to be less favorable in TiO_2−water than in bulk water. The DPMD simulations predict a larger dissolution barrier (Figure 2b), whereas the kinetic modeling gives a slower radius decay. The good agreement between the modeling which introduces the electrostatic contribution (Equation 3) and the DPMD simulation supports well the dominant role of interfacial charge in stabilizing nanobubble near the TiO_2 surface, which is mainly from bulk OH^- produced via the TiO_2 surface reactions and reduces the driving force for gas outflux.

Experimental Validation of the Anatase-Surface Effect on Nanobubble Evolution

We further experimentally validated the effect of the anatase-surface on nanobubble evolution. Figure 7a,b present representative dark-field snapshots showing the scattering features of bulk nanobubbles in pure water and of the mixed system containing both nanobubbles and anatase TiO_2 nanoparticles, respectively. As quantified in Figure 7c, the equilibrium number concentrations of bulk nanobubbles and TiO_2 nanoparticles in their individual suspensions are 0.997 × 10^8 and 0.210 × 10^8 mL^{-1}, respectively. After introducing the nanoparticles into the nanobubble suspension, the number concentration of the mixed system increases markedly to 1.655 × 10^8 mL^{-1}, which significantly exceeds the simple arithmetic sum of the concentrations measured in the isolated nanobubble and nanoparticle systems.

As illustrated in Figure 7e, in the presence of anatase, the mean diameter (d_{50}) of the dispersed substances increased from 302 to 327 nm. The pronounced enhancement of the number concentration together with the observed larger mean diameter for nanobubble indicates that TiO_2 nanoparticles may reduce nanobubble decay rather than merely contributing their own scattering signatures. This experimental trend aligns well with our simulation results shown in Figure 2 and in Table 1. The computed free-energy barrier for nanobubble dissolution is higher by approximately 42 kJ mol^{-1} near the anatase (101)−water interface than in bulk water. This substantially higher barrier in the vicinity of TiO_2 indicates enhanced dynamic stability of nanobubbles once formed, which is also qualitatively consistent with the theoretical kinetics analysis shown in Figure 6c.

Figure 7d shows that the measured zeta potential of bulk nanobubbles is −24.4 mV in pure water and −29.6 mV in the NB+TiO_2 suspensions. The simulation predicts a zeta potential of −2.7 mV for the N_2 nanobubble in the TiO_2−water system (Figure 6a), which is about 1 order of magnitude lower in absolute value than the experimental measurement. This difference might arise partially because the simulated nanobubbles are only about 3 nm in diameter, whereas the experimental nanobubbles exceed 100 nm. We attribute the more negative zeta potential in the TiO_2 suspensions to ionic contributions from both the anatase surface and the bulk water. The simulated TiO_2−water system shows the presence of OH^-

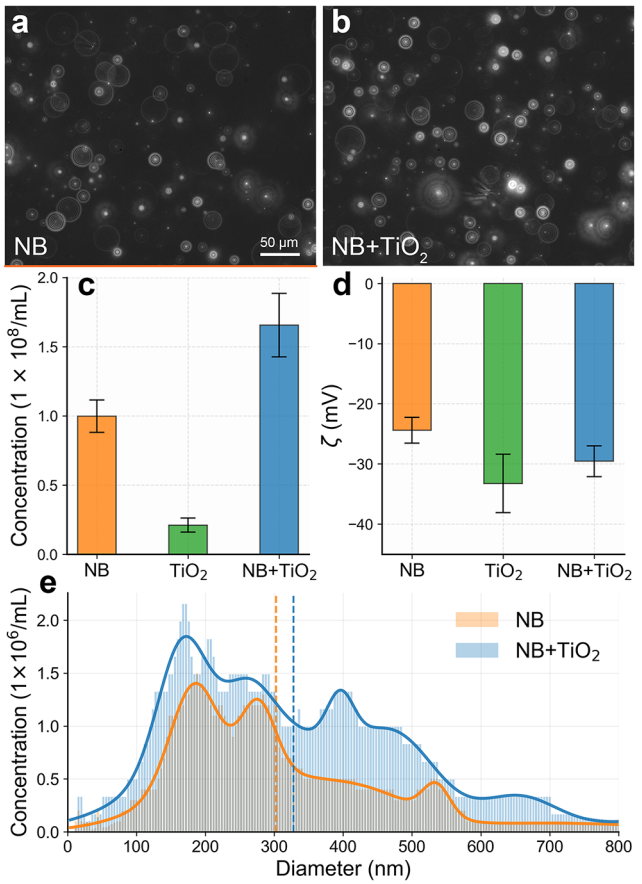

Figure 7. Experimental characterization of nanobubble and nanoparticle suspensions. (a) Snapshots of bulk nanobubbles (NBs) in pure water, and (b) in anatase TiO_2 (labeled as NB+TiO_2) suspensions. (c) Number concentrations and (d) zeta potentials (ζ) of NBs and of the combined nanobubble−nanoparticle (NB+TiO_2) suspensions in water, with TiO_2-only suspensions as the control group. (e) Number concentration histogram as a function of diameter for bulk NB and NB+TiO_2 systems, where the dashed line marks the mean diameter (d_{50}) and the solid line shows the fitted distribution.

(surf) as well as OH^- (bulk). The OH^- (bulk) ions preferably enrich near the nanobubble surface, as illustrated in Figure 5, and increase the negative surface charge of nanobubble.[33] In addition, the zeta potential of pure TiO_2 nanoparticles is −33.3 mV, more negative than the zeta potential of nanobubble in the TiO_2 suspensions, consistent with the ionic distributions shown in Figure 3.

In summary, the present experimental evidence supports the main conclusion of simulations that the presence of TiO_2 surface improves nanobubble stability through ion-mediated modulation.

CONCLUSIONS

The present study provides an atomistic understanding of how the interfacial ionic environment and thermodynamic−dynamic coupling collectively determine the evolution of N_2 nanobubble near the anatase (101)−water interface. By enhanced-sampling DPMD simulations for nanobubbles in different anatase (101)−water/electrolyte interface systems, we show that the interfacial adsorption state of nanobubbles is thermodynamically favored, whereas detachment into the bulk is unfavorable. The anatase (101) surface promotes the water dissociation through undercoordinated titanium and oxygen

https://doi.org/10.1021/jacs.6c05480
J. Am. Chem. Soc. 2026, 148, 18507−18517

sites, which changes the local ionic environment and makes the neutral systems alkaline, the alkaline system more alkaline, and the acidic system close to neutral, thus influencing the stability and evolution dynamics of nanobubble near the anatase-water interface. Compared with anatase-free systems, the nucleation barriers of nanobubbles are increased in all systems with the anatase (101) surface, but are less relevant for the acid−base strength. The nucleation barriers follow the qualitative order TiO_2−HCl ≳ TiO_2−NaOH ≳ TiO_2−water > TiO_2−NaCl. The much lower nucleation barrier in the anatase-saline system is a result of the salting-out effect. Because free OH^- ions generated by the surface reaction of anatase accumulate in the water layer near the nanobubble surface, we observe an approximate pH-dependence of negative zeta potentials of nanobubbles in the anatase-containing systems, except for the anatase-saline system. In the TiO_2−NaCl system, Na^+ and Cl^- ions, which also populate mainly near the nanobubble surface, screen the interfacial OH^- layer, so that a less negative zeta potential is obtained than that in the TiO_2−HCl. The dissolution barrier of nanobubble is linearly correlated with the magnitude of the zeta potential, that is, a more negative zeta potential corresponds to a higher barrier to nanobubble dissolution. These results are further supported by Epstein−Plesset modeling and experimental observations.

Despite these mechanistic insights, several limitations should be noted. The simulated nanobubbles consist of a limited number of molecules and have a diameter of just a few nanometers, much smaller than typical experimental nanobubbles (∼100 nm). Moreover, because nucleation is simulated in a finite system, the free energy profile can decrease beyond the barrier to a minimum at a finite cluster size, rather than approaching the asymptotic behavior expected from macroscopic classical nucleation theory.[84] In addition, nuclear quantum effects were not included, and the deep potential model employed short-range approximations without explicit long-range electrostatics. While these simplifications may lead to modest quantitative differences, they do not affect the central mechanistic insights or the core conclusions of this work.

■ ASSOCIATED CONTENT

Data Availability Statement

The requisite input files for replicating the research can be accessed at https://github.com/Zhang-pchao/research/tree/main/OPES-DPMD-Bubble-TiO2.

Supporting Information

The Supporting Information is available free of charge at https://pubs.acs.org/doi/10.1021/jacs.6c05480.

Details of potential model generation, including building data sets, DFT calculations and DP model training; details of enhanced sampling settings, including bias potential and collective variables, and free energy calculations; details of molecular dynamics simulations, identification of interfacial ionic species, construction of the transition matrix, as well as other discussions and information (PDF)

■ AUTHOR INFORMATION

Corresponding Authors

Chao Sun − *New Cornerstone Science Laboratory, Center for Combustion Energy, Department of Energy and Power Engineering, and Key Laboratory for Thermal Science and Power Engineering of Ministry of Education and Department of Engineering Mechanics, School of Aerospace Engineering, Tsinghua University, Beijing 100084, China;* orcid.org/0000-0002-0930-6343; Email: chaosun@tsinghua.edu.cn

Xuefei Xu − *New Cornerstone Science Laboratory, Center for Combustion Energy, Department of Energy and Power Engineering, and Key Laboratory for Thermal Science and Power Engineering of Ministry of Education, Tsinghua University, Beijing 100084, China;* orcid.org/0000-0002-2009-0483; Email: xuxuefei@tsinghua.edu.cn

Authors

Pengchao Zhang − *New Cornerstone Science Laboratory, Center for Combustion Energy, Department of Energy and Power Engineering, and Key Laboratory for Thermal Science and Power Engineering of Ministry of Education, Tsinghua University, Beijing 100084, China;* orcid.org/0000-0002-6556-6588

Yawen Gao − *New Cornerstone Science Laboratory, Center for Combustion Energy, Department of Energy and Power Engineering, and Key Laboratory for Thermal Science and Power Engineering of Ministry of Education, Tsinghua University, Beijing 100084, China;* orcid.org/0000-0002-9499-3765

Changsheng Chen − *New Cornerstone Science Laboratory, Center for Combustion Energy, Department of Energy and Power Engineering, and Key Laboratory for Thermal Science and Power Engineering of Ministry of Education, Tsinghua University, Beijing 100084, China;* orcid.org/0000-0003-2836-9160

Xiangdang Guo − *New Cornerstone Science Laboratory, Center for Combustion Energy, Department of Energy and Power Engineering, and Key Laboratory for Thermal Science and Power Engineering of Ministry of Education, Tsinghua University, Beijing 100084, China*

Complete contact information is available at: https://pubs.acs.org/10.1021/jacs.6c05480

Notes

The authors declare no competing financial interest.

■ ACKNOWLEDGMENTS

This work was supported by the National Natural Science Foundation of China (No. 22473066), the National Natural Science Foundation of China Excellence Research Group Program for "Multiscale Problems in Nonlinear Mechanics" (No. 12588201), the National Key R&D Program of China (No. 2025YFF0511800), the New Cornerstone Science Foundation through the New Cornerstone Investigator Program and the XPLORER PRIZE, Sinopec Petroleum Exploration and Production Research Institute, the Creative Seed Fund of Shanxi Research Institute for Clean Energy of Tsinghua University, the Shui Mu Scholarship at Tsinghua University (2025SM043, 2024SM049), the China Postdoctoral Science Foundation (No. 2025M781787) and the National Natural Science Foundation of China (No. 52406254). The authors would like to acknowledge the discussions of data sets with Professor Christoph Schran, Professor Chunyi Zhang and Zhou Li. Computational resources were partially provided by the Open Source Supercomputing Center of S-A-I.

REFERENCES

(1) Angulo, A.; van der Linde, P.; Gardeniers, H.; Modestino, M.; Fernández Rivas, D. Influence of Bubbles on the Energy Conversion Efficiency of Electrochemical Reactors. *Joule* **2020**, *4*, 555−579.

(2) Li, M.; Xie, P.; Yu, L.; Luo, L.; Sun, X. Bubble Engineering on Micro-/Nanostructured Electrodes for Water Splitting. *ACS Nano* **2023**, *17*, 23299−23316.

(3) Weijs, J. H.; Seddon, J. R.; Lohse, D. Diffusive Shielding Stabilizes Bulk Nanobubble Clusters. *ChemPhysChem* **2012**, *13*, 2197−2204.

(4) Chen, Q.; Wiedenroth, H. S.; German, S. R.; White, H. S. Electrochemical Nucleation of Stable N_2 Nanobubbles at Pt Nanoelectrodes. *J. Am. Chem. Soc.* **2015**, *137*, 12064−12069.

(5) Chen, C.; Gao, Y.; Wang, F.; Sun, C. A Multiscale Model for Bubble Nucleation Thresholds on Solid Walls in the Presence of Nanometre-Sized Defects. *J. Fluid Mech.* **2025**, *1015*, A47.

(6) Yang, S.; Yuan, J.; Xie, P.; Li, B.; Li, M.; Zhou, D.; Luo, L.; Sun, X. Macroscopic Bubble Generation Promoted by Nanobubble Seeds as a Traceless Anti-Fluctuation Strategy for Water Splitting. *Nat. Commun.* **2025**, *16*, 5732.

(7) Dixit, A. K.; Das, A. K. Molecular Approach for Understanding the Stability, Collision, and Coalescence of Bulk Nanobubbles. *Langmuir* **2022**, *38*, 16122−16133.

(8) Zhang, Y.; Zhang, X.; Lohse, D. Why and When Merging Surface Nanobubbles Jump. *Phys. Rev. Lett.* **2025**, *135*, 194001.

(9) Park, S.; Liu, L.; Demirkır, Ç.; van der Heijden, O.; Lohse, D.; Krug, D.; Koper, M. T. Solutal Marangoni Effect Determines Bubble Dynamics During Electrocatalytic Hydrogen Evolution. *Nat. Chem.* **2023**, *15*, 1532−1540.

(10) Gao, Z.; Wu, W.; Sun, W.; Wang, B. Understanding the Stabilization of a Bulk Nanobubble: A Molecular Dynamics Analysis. *Langmuir* **2021**, *37*, 11281−11291.

(11) Feng, M.; Ma, X.; Zhang, Z.; Luo, K. H.; Sun, C.; Xu, X. How Sodium Chloride Extends Lifetime of Bulk Nanobubbles in Water. *Soft Matter* **2022**, *18*, 2968−2978.

(12) Li, Y.; Zhang, L.-W.; Wang, B. Role of Mutual Diffusion in the Dissolution Behavior of One Primary Bulk Gas Nanobubble in Liquid: A Molecular Dynamics Study. *Langmuir* **2023**, *39*, 7684−7693.

(13) Wang, S.; Lyu, F.; Zhang, Z.; Mao, X.; Wei, H.; Pan, J. Enhanced Stability of Bulk Hydrogen Nanobubbles at Elevated External Pressures. *Phys. Rev. Fluids* **2025**, *10*, 93605.

(14) Li, J.; Zhang, H.; Guo, Z.; Jiang, J.; Zhang, X.; Cao, D.; Zeng, X. C. Simulation Evidence of Nanobubble Clusters of Gas in Water: A Nanoscale Solvation Mechanism. *J. Am. Chem. Soc.* **2025**, *147*, 28748−28757.

(15) Hirakawa, H.; Hashimoto, M.; Shiraishi, Y.; Hirai, T. Photocatalytic Conversion of Nitrogen to Ammonia with Water on Surface Oxygen Vacancies of Titanium Dioxide. *J. Am. Chem. Soc.* **2017**, *139*, 10929−10936.

(16) Shi, Y.; Zhao, Z.; Yang, D.; Tan, J.; Xin, X.; Liu, Y.; Jiang, Z. Engineering Photocatalytic Ammonia Synthesis. *Chem. Soc. Rev.* **2023**, *52*, 6938−6956.

(17) Kang, Q.; Cao, J.; Zhang, Y.; Liu, L.; Xu, H.; Ye, J. Reduced TiO_2 Nanotube Arrays for Photoelectrochemical Water Splitting. *J. Mater. Chem. A* **2013**, *1*, 5766.

(18) Sanadi, P. D.; Chougale, R. K.; Malavekar, D. B.; Kim, J. H.; Masimukku, S.; Chang-Chien, G.-P.; Ling, Y.-C.; Kolekar, S. S.; Kamble, G. S. Efficient Hydrogen Evolution via Neutral Water Electrolysis Using Nanocrystalline TiO_2 Electrocatalyst. *Sci. Rep.* **2025**, *15*, 16074.

(19) Shen, G.; Zhang, X. H.; Ming, Y.; Zhang, L.; Zhang, Y.; Hu, J. Photocatalytic Induction of Nanobubbles on TiO_2 Surfaces. *J. Phys. Chem. C* **2008**, *112*, 4029−4032.

(20) Epstein, P. S.; Plesset, M. S. On the Stability of Gas Bubbles in Liquid-Gas Solutions. *J. Chem. Phys.* **1950**, *18*, 1505−1509.

(21) Ohgaki, K.; Khanh, N. Q.; Joden, Y.; Tsuji, A.; Nakagawa, T. Physicochemical Approach to Nanobubble Solutions. *Chem. Eng. Sci.* **2010**, *65*, 1296−1300.

(22) Liu, Y.; Zhang, X. A Unified Mechanism for the Stability of Surface Nanobubbles: Contact Line Pinning and Supersaturation. *J. Chem. Phys.* **2014**, *141*, 134702.

(23) Chan, C. U.; Chen, L.; Arora, M.; Ohl, C.-D. Collapse of Surface Nanobubbles. *Phys. Rev. Lett.* **2015**, *114*, No. 114505.

(24) Azevedo, A.; Etchepare, R.; Calgaroto, S.; Rubio, J. Aqueous Dispersions of Nanobubbles: Generation, Properties and Features. *Miner. Eng.* **2016**, *94*, 29−37.

(25) Nirmalkar, N.; Pacek, A.; Barigou, M. On the Existence and Stability of Bulk Nanobubbles. *Langmuir* **2018**, *34*, 10964−10973.

(26) Li, M.; Ma, X.; Eisener, J.; Pfeiffer, P.; Ohl, C.-D.; Sun, C. How Bulk Nanobubbles Are Stable Over a Wide Range of Temperatures. *J. Colloid Interface Sci.* **2021**, *596*, 184−198.

(27) Ma, X.; Li, M.; Pfeiffer, P.; Eisener, J.; Ohl, C.-D.; Sun, C. Ion Adsorption Stabilizes Bulk Nanobubbles. *J. Colloid Interface Sci.* **2022**, *606*, 1380−1394.

(28) Yuan, L.; Raza, A.; AlMarzooqi, F.; Zhang, T. Efficient Alkaline Oxygen Evolution at Industrial Current Densities with Hierarchical Electrode Architecture Overcoming Mass Transport Limitations. *ACS Appl. Energy Mater.* **2025**, *8*, 13306−13317.

(29) Liu, Y.; Zhang, X. Nanobubble Stability Induced by Contact Line Pinning. *J. Chem. Phys.* **2013**, *138*, No. 014706.

(30) Weijs, J. H.; Lohse, D. Why Surface Nanobubbles Live for Hours. *Phys. Rev. Lett.* **2013**, *110*, No. 054501.

(31) Liu, Y.; Wang, J.; Zhang, X.; Wang, W. Contact Line Pinning and the Relationship between Nanobubbles and Substrates. *J. Chem. Phys.* **2014**, *140*, No. 054705.

(32) Tan, B. H.; An, H.; Ohl, C.-D. Resolving the Pinning Force of Nanobubbles with Optical Microscopy. *Phys. Rev. Lett.* **2017**, *118*, No. 054501.

(33) Zhang, P.; Chen, C.; Feng, M.; Sun, C.; Xu, X. Hydroxide and Hydronium Ions Modulate the Dynamic Evolution of Nitrogen Nanobubbles in Water. *J. Am. Chem. Soc.* **2024**, *146*, 19537−19546.

(34) Ushikubo, F. Y.; Enari, M.; Furukawa, T.; Nakagawa, R.; Makino, Y.; Kawagoe, Y.; Oshita, S. Zeta-Potential of Micro-and/or Nano-Bubbles in Water Produced by Some Kinds of Gases. *IFAC Proc.* **2010**, *43*, 283−288.

(35) Oh, S. H.; Kim, J.-M. Generation and Stability of Bulk Nanobubbles. *Langmuir* **2017**, *33*, 3818−3823.

(36) Zhou, L.; Wang, S.; Zhang, L.; Hu, J. Generation and Stability of Bulk Nanobubbles: A Review and Perspective. *Curr. Opin. Colloid Interface Sci.* **2021**, *53*, No. 101439.

(37) Kim, J.-Y.; Song, M.-G.; Kim, J.-D. Zeta Potential of Nanobubbles Generated by Ultrasonication in Aqueous Alkyl Polyglycoside Solutions. *J. Colloid Interface Sci.* **2000**, *223*, 285−291.

(38) Meegoda, J. N.; Aluthgun Hewage, S.; Batagoda, J. H. Stability of Nanobubbles. *Environ. Eng. Sci.* **2018**, *35*, 1216−1227.

(39) Wang, M.; Liu, S.; Ji, H.; Yang, T.; Qian, T.; Yan, C. Salting-Out Effect Promoting Highly Efficient Ambient Ammonia Synthesis. *Nat. Commun.* **2021**, *12*, 3198.

(40) Khairy, M.; Kubelka, J.; Piri, M. The Effects of Ionic Strength and pH on Nanobubble Electrostatic Stability in Saline Solutions. *Langmuir* **2025**, *41*, 22116−22128.

(41) Nirmalkar, N.; Pacek, A.; Barigou, M. Interpreting the Interfacial and Colloidal Stability of Bulk Nanobubbles. *Soft Matter* **2018**, *14*, 9643−9656.

(42) Calegari Andrade, M. F.; Ko, H.-Y.; Zhang, L.; Car, R.; Selloni, A. Free Energy of Proton Transfer at the Water-TiO_2 Interface from *Ab Initio* Deep Potential Molecular Dynamics. *Chem. Sci.* **2020**, *11*, 2335−2341.

(43) Zeng, Z.; Wodaczek, F.; Liu, K.; Stein, F.; Hutter, J.; Chen, J.; Cheng, B. Mechanistic Insight on Water Dissociation on Pristine Low-Index TiO_2 Surfaces from Machine Learning Molecular Dynamics Simulations. *Nat. Commun.* **2023**, *14*, 6131.

(44) Zhang, C.; Calegari Andrade, M. F.; Goldsmith, Z. K.; Raman, A. S.; Li, Y.; Piaggi, P. M.; Wu, X.; Car, R.; Selloni, A. Molecular-Scale Insights into the Electrical Double Layer at Oxide-Electrolyte Interfaces. *Nat. Commun.* **2024**, *15*, 10270.

https://doi.org/10.1021/jacs.6c05480
J. Am. Chem. Soc. 2026, 148, 18507−18517

(45) Schlegel, S. J.; Hosseinpour, S.; Gebhard, M.; Devi, A.; Bonn, M.; Backus, E. H. G. How Water Flips at Charged Titanium Dioxide: An SFG-study on the Water−TiO_2 Interface. *Phys. Chem. Chem. Phys.* **2019**, *21*, 8956−8964.
(46) Bischoff, M.; Kim, N. Y.; Joo, J. B.; Marchioro, A. Water Orientation at the Anatase TiO_2 Nanoparticle Interface: A Probe of Surface pKa Values. *J. Phys. Chem. Lett.* **2022**, *13*, 8677−8683.
(47) Ma, X.; Li, M.; Xu, X.; Sun, C. On the Role of Surface Charge and Surface Tension Tuned by Surfactant in Stabilizing Bulk Nanobubbles. *Appl. Surf. Sci.* **2023**, *608*, No. 155232.
(48) Li, Y.; Sun, T.; Cai, J.; Wang, B.; Li, M. Aging Dynamics of Bulk Nanobubbles under Pressure Oscillations. *J. Colloid Interface Sci.* **2025**, *708*, No. 139757.
(49) de Grotthuss, C. J. T. Mémoire sur la Décomposition de l'Eau et des Corps qu'elle Tient en Dissolution à l'Aide de l'Électricité Galvanique. *Ann. Chim.* **1806**, 54−74.
(50) Marx, D. Proton Transfer 200 Years After von Grotthuss: Insights from *Ab Initio* Simulations. *ChemPhysChem* **2006**, *7*, 1848−1870.
(51) Zhang, P.; Feng, M.; Xu, X. Double-Layer Distribution of Hydronium and Hydroxide Ions in the Air−Water Interface. *ACS Phys. Chem. Au* **2024**, *4*, 336−346.
(52) Wang, H.; Zhang, L.; Han, J. E. W. DeePMD-kit: A Deep Learning Package for Many-Body Potential Energy Representation and Molecular Dynamics. *Comput. Phys. Commun.* **2018**, *228*, 178−184.
(53) Zeng, J.; et al. DeePMD-kit v2: A Software Package for Deep Potential Models. *J. Chem. Phys.* **2023**, *159*, No. 054801.
(54) Zhang, P.; Gardini, A. T.; Xu, X.; Parrinello, M. Intramolecular and Water Mediated Tautomerism of Solvated Glycine. *J. Chem. Inf. Model.* **2024**, *64*, 3599−3604.
(55) Zhang, P.; Xu, X. Propensity of Water Self-Ions at Air(Oil)−Water Interfaces Revealed by Deep Potential Molecular Dynamics with Enhanced Sampling. *Langmuir* **2025**, *41*, 3675−3683.
(56) Zhang, P.; Xu, X. Modulation of Electric Field and Interface on Competitive Reaction Mechanisms. *J. Chem. Theory Comput.* **2025**, *21*, 6584−6593.
(57) Zhang, B.; Zhang, P.; Xu, X. Solvent Effect on the Electrocatalytic Nitrogen Reduction Reaction: A Deep Potential Molecular Dynamics Simulation with Enhanced Sampling for the Case of the Ruthenium Single Atom Catalyst. *J. Mater. Chem. A* **2026**, *14*, 7109−7120.
(58) Zeng, J.; et al. DeePMD-kit v3: A Multiple-Backend Framework for Machine Learning Potentials. *J. Chem. Theory Comput.* **2025**, *21*, 4375−4385.
(59) Sun, J.; Ruzsinszky, A.; Perdew, J. P. Strongly Constrained and Appropriately Normed Semilocal Density Functional. *Phys. Rev. Lett.* **2015**, *115*, No. 036402.
(60) Kresse, G.; Furthmüller, J. Efficient Iterative Schemes for *Ab Initio* Total-Energy Calculations Using a Plane-Wave Basis Set. *Phys. Rev. B* **1996**, *54*, 11169.
(61) Kresse, G.; Furthmüller, J. Efficiency of *Ab Initio* Total Energy Calculations for Metals and Semiconductors Using a Plane-Wave Basis Set. *Comput. Mater. Sci.* **1996**, *6*, 15−50.
(62) Lu, D.; Jiang, W.; Chen, Y.; Zhang, L.; Jia, W.; Wang, H.; Chen, M. DP Compress: A Model Compression Scheme for Generating Efficient Deep Potential Models. *J. Chem. Theory Comput.* **2022**, *18*, 5559−5567.
(63) Torrie, G.; Valleau, J. Nonphysical Sampling Distributions in Monte Carlo Free-Energy Estimation: Umbrella Sampling. *J. Comput. Phys.* **1977**, *23*, 187−199.
(64) Invernizzi, M.; Parrinello, M. Rethinking Metadynamics: From Bias Potentials to Probability Distributions. *J. Phys. Chem. Lett.* **2020**, *11*, 2731−2736.
(65) Invernizzi, M.; Parrinello, M. Exploration vs Convergence Speed in Adaptive-Bias Enhanced Sampling. *J. Chem. Theory Comput.* **2022**, *18*, 3988−3996.
(66) Ray, D.; Rizzi, V. Enhanced Sampling with Suboptimal Collective Variables: Reconciling Accuracy and Convergence Speed. *J. Chem. Theory Comput.* **2025**, *21*, 58−69.
(67) Tribello, G. A.; Bonomi, M.; Branduardi, D.; Camilloni, C.; Bussi, G. PLUMED 2: New Feathers for an Old Bird. *Comput. Phys. Commun.* **2014**, *185*, 604−613.
(68) Tribello, G. A.; Giberti, F.; Sosso, G. C.; Salvalaglio, M.; Parrinello, M. Analyzing and Driving Cluster Formation in Atomistic Simulations. *J. Chem. Theory Comput.* **2017**, *13*, 1317−1327.
(69) Plimpton, S. Fast Parallel Algorithms for Short-Range Molecular Dynamics. *J. Comput. Phys.* **1995**, *117*, 1−19.
(70) Martínez, L.; Andrade, R.; Birgin, E. G.; Martínez, J. M. PACKMOL: A Package for Building Initial Configurations for Molecular Dynamics Simulations. *J. Comput. Chem.* **2009**, *30*, 2157−2164.
(71) Calegari Andrade, M.; Car, R.; Selloni, A. Probing the Self-Ionization of Liquid Water With *Ab Initio* Deep Potential Molecular Dynamics. *Proc. Natl. Acad. Sci. U. S. A.* **2023**, *120*, No. e2302468120.
(72) Nosé, S. A Unified Formulation of the Constant Temperature Molecular Dynamics Methods. *J. Chem. Phys.* **1984**, *81*, 511−519.
(73) Hoover, W. G. Canonical Dynamics: Equilibrium Phase-Space Distributions. *Phys. Rev. A* **1985**, *31*, 1695.
(74) Gao, Y.; Chen, C.; Wang, F.; Li, M.; Sun, C. Characterization and Removal of Contaminants in Lithography. *Sci. China Phys. Mech. Astron.* **2025**, *68*, 294702.
(75) Gao, Y.; Zhang, P.; Luo, H.; Chen, C.; Niu, J.; Tang, Y.; Wang, R.; Li, M.; Xu, X.; Sun, C. Thermal Response of Nanobubble Suspensions under Freeze-Thaw Cycles through Experiment and Molecular Dynamics Simulations. *ACS Appl. Mater. Interfaces* **2025**, *17*, 67284−67294.
(76) Gao, Y.; Chen, C.; Li, M.; Sun, C. Ionic Environment-Modulated Nucleation and Stability of Multiscale Nanodomains in Surfactant-Free Microemulsions. *J. Colloid Interface Sci.* **2025**, *696*, No. 137833.
(77) Svetovoy, V. B.; Dević, I.; Snoeijer, J. H.; Lohse, D. Effect of Disjoining Pressure on Surface Nanobubbles. *Langmuir* **2016**, *32*, 11188−11196.
(78) Mazumder, M.; Bhushan, B. Propensity and Geometrical Distribution of Surface Nanobubbles: Effect of Electrolyte, Roughness, pH, and Substrate Bias. *Soft Matter* **2011**, *7*, 9184−9196.
(79) Gallo, M.; Magaletti, F.; Casciola, C. M. Heterogeneous Bubble Nucleation Dynamics. *J. Fluid Mech.* **2021**, *906*, A20.
(80) Zhang, H.; Guo, Z.; Zhang, X. Surface Enrichment of Ions Leads to the Stability of Bulk Nanobubbles. *Soft Matter* **2020**, *16*, 5470−5477.
(81) Ke, S.; Xiao, W.; Quan, N.; Dong, Y.; Zhang, L.; Hu, J. Formation and Stability of Bulk Nanobubbles in Different Solutions. *Langmuir* **2019**, *35*, 5250−5256.
(82) Uchida, T.; Liu, S.; Enari, M.; Oshita, S.; Yamazaki, K.; Gohara, K. Effect of NaCl on the Lifetime of Micro- and Nanobubbles. *Nanomaterials* **2016**, *6*, 31.
(83) O'Neill, N.; Shi, B. X.; Fong, K.; Michaelides, A.; Schran, C. To Pair or Not to Pair? Machine-Learned Explicitly-Correlated Electronic Structure for NaCl in Water. *J. Phys. Chem. Lett.* **2024**, *15*, 6081−6091.
(84) Becker, R.; Döring, W. Kinetische Behandlung der Keimbildung in übersättigten Dämpfen. *Ann. Phys.* **1935**, *416*, 719−752.

https://doi.org/10.1021/jacs.6c05480
J. Am. Chem. Soc. 2026, 148, 18507−18517